Research Paper

Bismuth spheres assembled on graphene oxide: Directional charge transfer enhances plasmonic photocatalysis and *in situ* DRIFTS studies

Xinwei Li[a], Wendong Zhang[b], Wen Cui[a], Yanjuan Sun[a], Guangming Jiang[a,*], Yuxin Zhang[c], Hongwei Huang[d], Fan Dong[a,*]

[a] *Chongqing Key Laboratory of Catalysis and New Environmental Materials, Engineering Research Center for Waste Oil Recovery Technology and Equipment, College of Environment and Resources, Chongqing Technology and Business University, Chongqing, 400067, China*
[b] *Department of Scientific Research Management, Chongqing Normal University, Chongqing, 401331, China*
[c] *State Key Laboratory of Mechanical Transmissions, College of Materials Science and Engineering, Chongqing University, Chongqing, 400044, China*
[d] *Beijing Key Laboratory of Materials Utilization of Nonmetallic Minerals and Solid Wastes, National Laboratory of Mineral Materials, School of Materials Science and Technology, China University of Geosciences, Beijing 100083, China*

ARTICLE INFO

ABSTRACT

This work reports a facile approach to monodisperse bismuth nanospheres (Bi-NPs), which are then evenly assembled on graphene oxide (GO) via a solution-based sonication method. The resultant Bi-NPs@GO composite can serve as a robust direct plasmonic photocatalyst to remove 42.3% of ppb-level NO from a continuous flow under UV illumination. Localized surface plasmon resonance (LSPR) of Bi nanospheres were confirmed by a numerical simulations and the intense LSPR on Bi nanospheres under UV illumination accounts for the generation of energetic hot electron/hole pairs for NO removal. Experimental results combined with the density functional theory calculation analysis indicate that the abundant carboxyl groups on GO play crucial roles in whole photocatalysis: (i) form a directional carrier deliver channel: $Bi \rightarrow C_{graphene} \rightarrow C_{COOH} \rightarrow O_{COOH}$, facilitating the hot electrons transfer from the plasmonic Bi nanospheres to carboxyl groups and encouraging the carrier separation efficiency, (ii) enrich the reactant concentrations (O_2 and NO) around catalyst surface by adsorption, promoting the generation of active radicals $\cdot O_2^-$ and the sequent oxidation of NO. Further examination of the photocatalytic NO oxidation by *in situ* DRIFT confirms the key roles of carboxyl groups as adsorption/reaction centers for photocatalytic NO oxidation, as well as the pathway of NO oxidation to nontoxic nitrate on the catalyst.

1. Introduction

Photocatalysis constitutes one of the most active branches of heterogeneous catalysis and the designed synthesis of high-efficient photocatalyst is highly desired [1–3]. Plasmonic metals, featured by their unique localized surface plasmon resonance (LSPR) property, have emerged as one appealing class of photocatalysts with wide applications in environmental remediation [4,5]. In this LSPR-directed photocatalysis, the surface electrons of the plasmonic metals will easily oscillate resonated with the incident photon at an appropriate frequency, giving rise to a local electromagnetic field, the non-radiative decay of which will then trigger the generation of numbers of hot carriers for catalytic redox reactions [6–8]. The direct plasmonic photocatalysis is usually operated under a low-intense wave photon illumination, which enables a significant enhancement in kinetics of reactions [9]. However, current SPR-directed photocatalysis are limited

to the noble metal, such as Au and Ag [10–13], which restrict their practical application.

In our previous work, we found that the earth-abundant bismuth metal (Bi) also has a unique LSPR property, and more importantly, can serve as a direct plasmonic photocatalyst in ppb-level NO removal from a gas flow under UV illumination [14]. However, bare Bi particles usually suffer from a poor chemical stability, which hampers their use for SPR response. Moreover, the hot carriers produced via LSPR in Bi metal cannot travel over distances longer than tens of nanometers before losing their energy by radiative scattering [15]. As a result, a poor photocatalytic activity was achieved.

To improve the performance of Bi metals, two strategies were proposed in this work: (i) control the metallic Bi into the shape of uniform nanospheres (denoted as Bi-NPs), considering that Bi-NPs with a uniform shape and a large specific surface area have a much enhanced LSPR in the wavenumber range of 220–280 nm [16], and (ii) introduce

graphene oxide (GO) as the support for Bi-NPs. As we know, the 2D material GO has been widely used as a support for many photocatalysts, such as ZnO [17], TiO$_2$ [18], Ag$_3$PO$_4$ [19] and g-C$_3$N$_4$ [20]. The introduce of GO could usually increase both the dispersion of the photocatalyst and the photocarrier separation efficiency [21]. However, our work found that the abundant carboxyl groups on GO actually play more crucial roles: (i) form a unique channel: Bi-graphene-carboxyl group, facilitating the hot electrons transfer from the plasmonic Bi-NPs to carboxyl groups and encouraging the carrier transfer efficiency, (ii) enrich the reactant concentrations (such as O$_2$ and NO) around catalyst surface by adsorption, promoting the generation of active radicals $\cdot$O$_2^-$ and the sequent oxidation of NO. To our knowledge, these new functions of GO have never been reported.

Here, the Bi-NPs with uniform size and morphology were fabricated by a wet-chemical reduction method, which were then evenly assembled onto GO sheets under the assistant of intense sonication. The resultant composite (denoted as Bi-NPs@GO) is a robust plasmonic photocatalyst and could remove 42.3% NO removal in a continuous flow under UV illumination. LSPR feature of Bi nanospheres was presented by numerical simulations, and the function of GO was studied by the combination of experimental analysis and density functional theory calculations (DFT calculations). *In situ* Diffuse Reflectance Infrared Fourier-transform Spectroscopy (*in situ* DRIFTS) was applied to track the pathway of pollutant removal during the photocatalytic oxidation. Our results represent an important step in demonstrating the potential of Bi metal as a new direct plasmonic photocatalyst for achieving efficient solar energy conversion and environmental remediation systems.

2. Experimental

2.1. Materials

Bismuth chloride, PVP (Polyvinyl pyrrolidone), hydrazine hydrate, ethylene glycol, sodium hydroxide and ethyl alcohol were purchased from Sigma-Aldrich. GO with a BET surface area of 206.0 m^2/g was purchased from Nanjing Xianfeng Nano Company. All chemicals were analytical grade and used without further purification.

2.2. Sample preparations

In a typical synthesis, 0.158 g of bismuth chloride, 0.1 g sodium hydroxide, 276 mg PVP and 25 mL of ethylene glycol were mixed into a 50 mL three-neck flask and magnetically stirred under a N$_2$ atmosphere till a transparent light white solution was obtained. The resultant mixture was heated from room temperature to 190 °C, and then kept for a certain time. The reaction time was controlled for 0.5 h, 1.0 h and 2.0 h, respectively (the obtained samples were labeled as Bi-NPs-0.5, Bi-NPs-1 and Bi-NPs-2). Once cooled down to room temperature, Bi-NPs were collected by adding ethanol and centrifugation (5500 rpm, 3 min), and further purified with hydrazine monohydrate/ethanol to remove the surfactant [22], which was labeled as Bi-NPs-HW. The as-prepared Bi nanospheres powders and 0.05 g graphene oxide were dispersed in 5 mL and 50 mL ethanol by ultrasonication, respectively. The GO suspension was dropwise added into Bi NP solution and stirred for 60 min to obtain Bi-NPs@GO composite. The composite was collected by centrifugation and further subjected to a hydrazine-washing to remove the surfactant. The as-prepared samples were labeled as Bi-NPs@GO. The process is illustrated in Fig. 1.

2.3. Characterization

The crystal phases of the sample were analyzed by X-ray diffraction (XRD) with Cu Kα radiation (model D/max RA, Rigaku Co., Japan). Fouriertransform infrared (FT-IR) spectra were recorded on a Nicolet Nexusspectrometer on samples embedded in KBr pellets. Scanning electron microscopy (SEM; model JSM-6490, JEOL, Japan) and

transmission electron microscopy (TEM; JEM-2010, Japan) were used to characterize the morphology and structure of the obtained products. The UV–vis diffuse-reflectance spectrometry (DRS) spectra were obtained for the dry-pressed disk samples using a Scan UV–vis spectrophotometer (TU-1901, China) equipped with an integrating sphere assembly, using 100% BaSO$_4$ as the reflectance sample. Nitrogen adsorption–desorption isotherms were obtained on a nitrogen adsorption apparatus (ASAP 2020, USA). All the samples were degassed at 100 °C prior to measurements. The sample for electron spin resonance (ESR) measurement was prepared by mixingBi-NPs@GO in a 50 mL DMPO solution tank, respectively (aqueous dispersion for DMPO-$\cdot$OH and methanol dispersion for DMPO-$\cdot$O$_2^-$). The photocurrent response measurements were performed in three-electrode quartz cells with a 0.1 M Na$_2$SO$_4$ electrolyte solution. Platinum wire was used as the counter electrode, and saturated calomel electrodes were used as the reference electrodes. Bi-NPsand Bi-NPs@GO film electrodes on ITO served as the working electrode, separately. The photoelectrochemical experiment results were recorded using an electrochemical system (CHI-660B, China).

2.4. Evaluation of photocatalytic activity

The photocatalytic activity was evaluated by measuring its efficiency for ppb-level NO removal in a continuous flow reactor at room temperature. The rectangular reactor, made of stainless steel and covered with Saint-Glass, has a volume capacity of 4.5 L (30 cm × 15 cm × 10 cm). A 15 W UV lamp with wavelength range of 280–320 nm is vertically placed on top of the reactor. The photocatalyst (0.2 g) was dispersed into 15 mL of ethanol via the sonication and then painted onto the bottom of two culture dishes (made of glass, 12.0 cm in diameter). Then, the dishes are vacuum dried and placed at the center of the reactor. NO gas is supplied by a compressed gas cylinder with a concentration of 100 ppm (N$_2$ balance), which is further diluted to 500 ppb by the air stream. The desired relative humidity level in NO flow was controlled at 50% by passing the zero air streams through a humidification chamber. A gas blender premixed the gas streams completely, and a mass flow controller was used to control the flow rate at 2.4 L min^{-1}. The lamp was turned on once the adsorption-desorption equilibrium was achieved. One chemiluminescence NO analyzer (Thermo Environmental Instruments Inc., 42i-TL) continuously measured the NO concentration at a sampling rate of 1.0 L min^{-1}. The removal efficiency (η) was calculated as η (%) = (1 − C/C$_0$) × 100%, where C and C$_0$ are the NO concentrations in the outlet and feeding stream, respectively.

2.5. In situ DRIFTS investigation on photocatalytic NO oxidation

In situ DRIFTS measurements were conducted using the TENSOR II FT-IR spectrometer (Bruker) equipped with an *in situ* diffuse-reflectance cell (Harrick) and a high temperature reaction chamber (HVC). The reaction chamber equipped with three gas ports and two coolant ports. High-purity He, high-purity O$_2$ and 100 ppm of NO (in He) mixture can be fed into the reaction system and a three-way ball valve is used to switch the target gas (NO) and purge gas (He). The total gas flow rate was 100 mL min^{-1} and the concentration of NO is 50 ppm by the dilution of O$_2$. The chamber is enclosed with a dome with three windows, two for IR light entrance and detection, and one for illuminating of the photocatalyst. The observation window is UV quartz and ZnSe for the other two windows. And High Pressure Mercury lamp (MVL-210, Optpe, Japan) was used for UV light source.

2.6. DFT calculations

Spin-polarized DFT-D2 [23] calculations were carried out utilizing the "Vienna ab initio simulation package" (code VASP5.4) [24,25], which uses a generalized gradient correlation functional [26]. A plane-
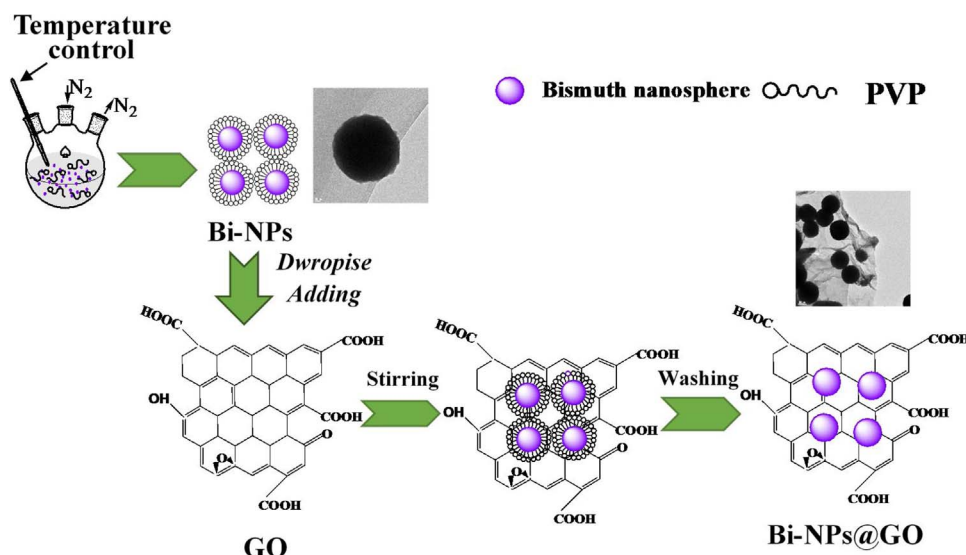
wave basis set with energy cut off at 400 eV with the framework of the projector-augmented wave method was conducted, setting the Gaussian smearing width to 0.2 eV [27,28]. The Brillouin zone was sampled with a $3 \times 3 \times 1$ K points. All atoms were allowed to converge to 0.01 eV Å^{-1} A $3 \times 3 \times 1$ supercell of graphene including 72C atoms was employed first. Then a single Bi atom was supported at the center of a 5-8-5 vacancy defect that offers appropriate space for the Bi stabilization [29,30]. The calculated bond lengths are consistent with the publish values [31].

3. Results and discussion

3.1. Synthesis of Bi-NPs@GO photocatalysts

Monodisperse Bi-NPs were synthesized in a hot ethylene glycol solution with bismuth chloride as the precursor and PVP as the surfactant. In this system, ethylene glycol not only acts as a solvent, but also a reducing agent to convert Bi^{3+} to Bi^0. PVP tends to be adsorbed on the surface of Bi-NPs, regulating the crystallization of Bi into the shape of uniform nanospheres and simultaneously preventing their aggregation. Fig. 1a presents a typical SEM image of the as-synthesized Bi-NPs which shows uniformly in size of ~200 nm and shape of sphere. The reaction time-dependent morphological evolution of Bi-NPs was investigated and the results in Fig. S1 show that a longer reaction time will generate some nanograins and increase the possibility of particle aggregation. The TEM image in Fig. 2b again presents the regular size of Bi-NPs around 200–250 nm. Further HRTEM examination in Fig. 2c finds the ordered lattice fringes in the core of Bi-NPs with a spacing of ~0.328 nm and a 2–3 nm-thick shell with no lattice fringes. The lattice spacing of ~0.328 nm matched well with the (012) atomic planes of Bi phase, confirming the formation of metallic Bi-NPs. Since Bi phase can be easily oxidized when exposed to air under room temperature, this

shell with no crystallographic periodicity should be the amorphous bismuth oxide (BiO$_x$). These BiO$_x$ shell could shield the Bi-NPs from further oxidation, and maintain the performance of the metallic Bi nanospheres [32].

The as-synthesized Bi-NPs were then deposited onto GO via a solution-based sonication method (See the procedure in Experimental Section). Since Bi-NPs were capped with the surfactant PVP, which may hinder electron transfer between Bi-NPs and the reactants [33,34]. A hydrazine-based washing procedure was then employed to remove the PVP (See the procedure in Experimental Section). To probe the surface group difference between Bi nanospheres before (Bi-NPs) and after (Bi-NPs-HW) wash, infrared adsorption spectra were conducted. The results in Fig. 3c show that the as-synthesized Bi-NPs have three peaks at 1663, 1427, 1288 cm^{-1}, which could be assigned to the free C=O stretching band, pyrrole and N–H–O complex of PVP [35]. These three peaks totally disappear on the IR spectrum of Bi nanospheres after the hydrazine wash, confirming the high efficiency of hydrazine in washing away the PVP. The removal of PVP could also enhance the connection between Bi-NPs and GO, which will facilitate the carrier delocalization. Fig. 3a,b and Fig. S2 show the TEM images of as-prepared Bi-NPs@GO sample, where the Bi nanospheres are uniformly deposited on GO and less change in size and shape on Bi nanospheres are observed. It can be concluded that, the surfactant-removing washing procedure cannot substantially affect quality of Bi-NPs. Infrared adsorption spectra of Bi-NPs@GO were also investigated in Fig. 3c. Obviously, no peak for PVP is detected, but some newly peaks at around 1375 and 1635 cm^{-1} emerge, which could be indexed to the sp^2-hybridized C=C in plane stretching and carboxyl groups on GO, respectively [36,37]. It implies that abundant carboxyl groups exist in Bi-NPs@GO [38–40]. The characteristic peak located at 845 cm^{-1} corresponds to stretching vibrations of Bi-O [41], which also suggests the formation of amorphous BiO$_x$ layer on the surface. However, the intensity for Bi-O is barely weak
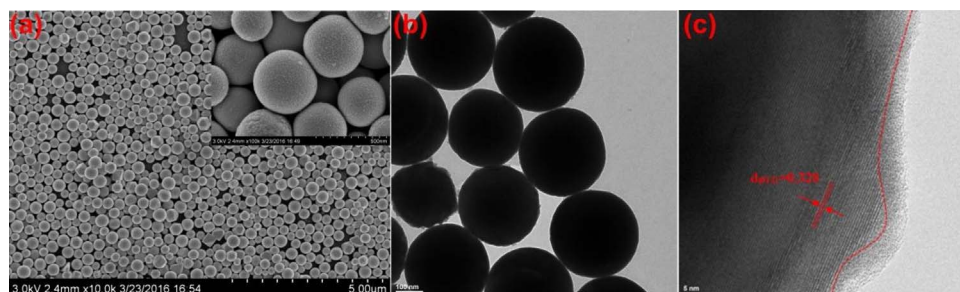

Fig. 2. SEM (a), TEM (b) and HRTEM(c) images of Bi-NPs-1.
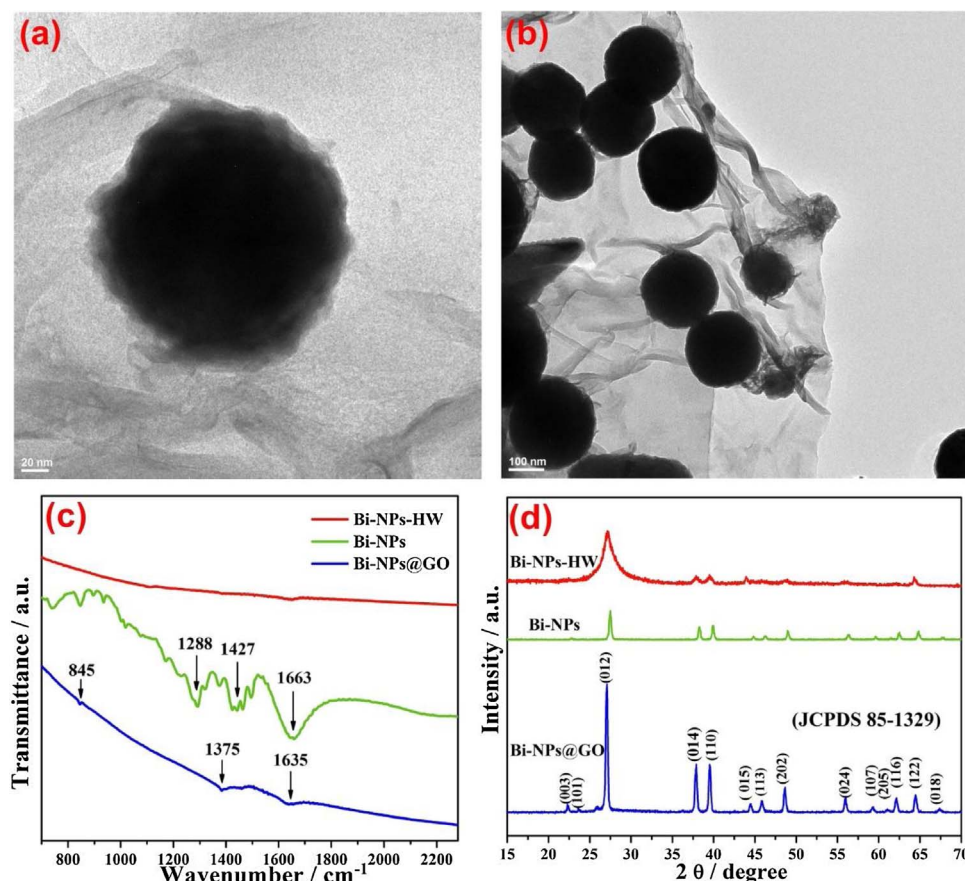
Fig. 3. TEM image of Bi-NPs@GO (a, b), FT-IR (c) and XRD patterns (d) of Bi-NPs, Bi-NPs-HW and Bi-NPs@GO.

due to the very low contents of BiO_x.

The powder X-ray diffraction (XRD) patterns of Bi-NPs, Bi-NPs-HW and Bi-NPs@GO are illustrated in Fig. 3d. All the samples exhibit nearly the same peaks at 22.3°, 23.7°, 27.3°, 37.9°, 39.5°, 44.6°, 45.9°, 48.7°, 56.0°, 59.2°, 61.0°, 62.1°, 64.4° and 67.4° which can all be assigned to the orthorhombic phase of Bi metal (JCPDS 85–1329). Bi-NPs@GO sample exhibits sharper diffraction peaks, which can be indexed as (012), (014), (110), (015), (113), (202) crystalline planes of Bi metal, respectively. Because of the Bi-NPs homogeneously deposited on GO avoiding aggregation effectively, the crystallinity degree is increased to a certain extent, similar results were observed in Tang's study [42]. Additionally, no obvious typical diffraction peaks of GO can be observed, possibly due to the shielding effect of strong diffraction signals from Bi nanospheres and the low amount of GO [43–45].

Specific surface areas of Bi-NPs@GO are determined to be 12.3 $m^2 g^{-1}$, much larger than 4.3 $m^2 g^{-1}$ of Bi-NPs, as surface area of GO is 206.0 m^2/g, the enlarged surface area should arise from the introduction of GO and the improved dispersion of Bi-NPs on GO. The typical IV isotherms of all the samples and a high adsorption at relatively high pressure (P/P^0) range (approaching 1.0) (Fig. 4a) indicates the presence of mesopores and macropores. Besides, the isotherms exhibit H3 hysteresis loop, indicating the presence of slit-shaped pores. The corresponding pore-size distributions of the samples Fig. 4b suggest that all the samples exhibit broad pore-size distributions of 10–100 nm. More detailed, Bi-NPs@GO have a peak pore diameter distribution at 2–3 nm. The high specific surface area and the abundant pores in Bi-NPs@GO should promote the gathering of pollutants around photocatalyst surface, which is favorable for the pollutant removal.

3.2. Photocatalytic NO removal

The photocatalytic performance of GO, Bi-NPs, Bi-NPs-HW and Bi-NPs@GO for NO removal from a continuous air flow were then tested under UV illumination, and the activity was assessed by the ratio of NO concentration in outlet streams (C) to that in feeding streams (C_0). The results in Fig. 5a show that GO is inertness, while the unwashed Bi-NPs has a weak efficiency of only about 8.2% [efficiency calculated by $(1 - C/C_0) \times 100\%$] as the surface surfactant would block the carrier
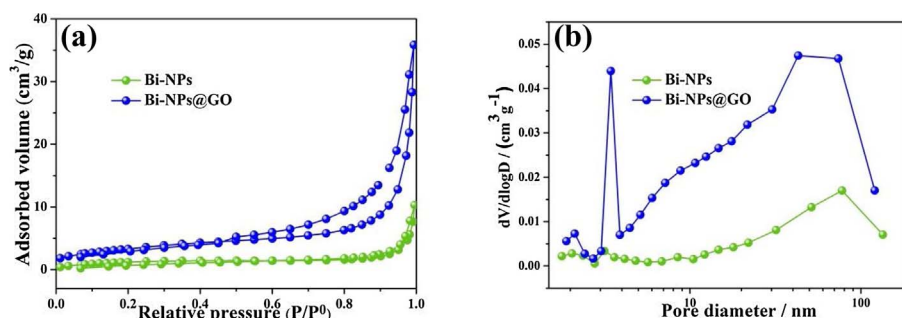

Fig. 4. N_2 adsorption-desorption isotherm (a) and the corresponding pore distribution (b) of Bi-NPs and Bi-NPs@GO.
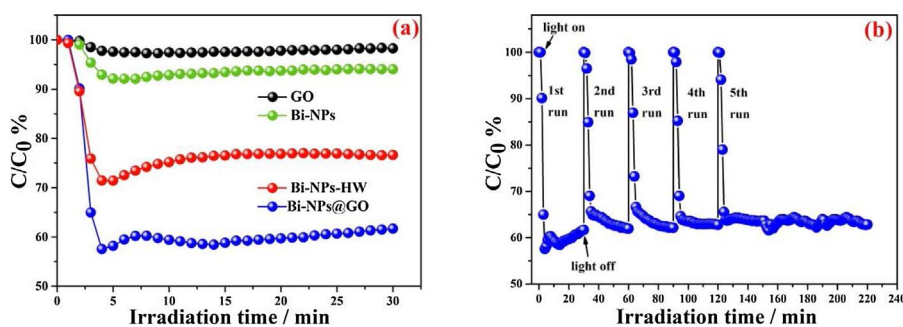
Fig. 5. Comparison of the UV light photocatalytic performance over Bi-NPs, Bi-NPs-HW, Bi-NPs@GO and GO (a) and the cycling test of Bi-NPs@GO (b).

transfer to ambient gas molecules for reaction. After hydrazine washing procedure, Bi-NPs-HW has a high initial efficiency of 30.2% but retain only 22.7% after a 30 min test, indicating the poor durability of the bare Bi nanospheres. After depositing Bi nanospheres on GO, the resultant Bi-NPs@GO exhibits a much enhanced activity to 42.3%, and also a much improved durability as little decrease in the removal efficiency after at least 5 cycles (Fig. 5b). The fifth durability test is prolonged to 100 min. Fig. S3 and Fig. S4 present the structure and morphology of Bi-NPs@GO after the durability test. It can be clearly observed that the Bi-NPs@GO is stable in microstructure under repeated irradiation and thus the photocatalytic activity can be well-maintained. All these demonstrate that Bi is the only active one for photocatalytic NO oxidation in Bi-NPs@GO photocatalyst, and the introduction of GO could improve both the activity and durability of Bi nanospheres.

3.3. Plasmonic feature of Bi-NPs

As indicated, Bi nanospheres are the only active ones in our Bi-NPs@GO system. The activity should arise from their unique LSPR feature. It enables Bi nanospheres to convert the incident photon energy into plasmon oscillations of the surface electrons, the sequent non-radiative decay of which will then produce energetic hot electrons for chemical reaction [6–8]. The LSPR property of Bi-NPs and Bi-NPs@GO were characterized by the UV absorption spectra, and the results in Fig. 6a present a strong absorption in the UV region around 280 nm in both the Bi-NPs and Bi-NPs@GO, which could be ascribed to the dominant LSPR absorption peak of Bi metal. However, Bi-NPs@GO presents a much higher absorption than Bi-NPs, possibly due to the homogeneous dispersion of Bi-NPs on GO as GO has a strong UV light absorption. To describe more clearly the LSPR intensity as well as the interaction between Bi nanospheres, a numerical simulation was further conducted to present the plasmon electromagnetism oscillations on Bi-NPs under 280 nm photon excitation (detailed parameter see supporting information). Based on TEM images as mentioned above (Fig. 3), both one 200 nm Bi nanosphere and two 200 nm Bi nanospheres with inter gap of 1 nm are shown in Fig. 6b. There is a clear

local electric field that is homogeneously exhibited around Bi nanosphere after light excitation. However, the electric field around the Bi particles is lower than that of in noble metal [46]. Notably, the intensity of local electromagnetic field of single Bi nanosphere is enhanced in that of the double counterparts, suggesting the adjacent local plasmon oscillations could be accumulated, thus hot carriers with high energy could be created for photocatalysis.

3.4. Role of GO

The introduction of GO could significantly improve the activity of Bi nanospheres. To offer a deeper understanding of the involved photocatalytic mechanism, DFT calculationsare employed to verify the change in electronic transfer approach after introducing GO. A $3 \times 3 \times 1$ supercell of graphene (GP) including 72C atoms was constructed. Carboxyls is added at the edge of graphene layer to get GO. Then, a single Bi atom was supported at the center of a 5-8-5 vacancy defect that offers appropriate sitesfor Bi nanosphere stabilization. There are clear covalent interactions between Bi and graphene carbon atoms from the side view of electric localization functional (ELF, Fig. 7a), and between graphene carbon atoms and carboxyl from the top view of ELF (Fig. 7b). The existence of those covalent interactions enable the build of a unique electron deliver chanel, denoted as Bi-graphene-carboxyl. The charge density difference (Fig. 7c,d) illustrates that graphene C atom, like an intermediate station, can draw charges from Bi atom and then transfer them to oxygen atoms in carboxyl. Thus in this electron deliver channel, the electrons actually flow in a fixed direction of $Bi \rightarrow C_{graphene} \rightarrow C_{COOH} \rightarrow O_{COOH}$. Accordingly during the SPR-directed photocatalysis on Bi-NPs@GO, the hot electrons produced via the decay of LSPR are inclined to transfer from Bi to the carboxyl groups, and thus the carboxyl groups actually serve as electron sinks.

During the LSPR non-radiatively decay, the photon energy is converted to single electron/hole pair occurring ~10 fs initial after plasmon excitations [7]. To see the channel effect on the carrier separation efficiency, the photocurrent-currents on Bi-NPs and Bi NP@GO under UV–vis lightwere investigated and compared (See the results shown in Fig. 7e). The obviously enhanced photocurrent of Bi-NPs@GO
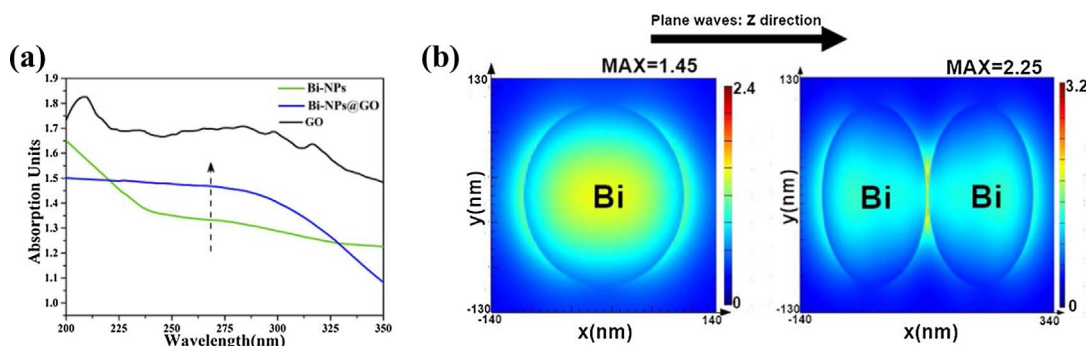

Fig. 6. UV absorption spectra of GO, Bi-NPs and Bi-NPs@GO (a) and Simulated spatial distribution of local electromagnetic field for Bi-NPs under 280 nm photon excitation around one 200 nm Bi NP and two 200 nm NPs with an inter-particle gap of 1 nm (b).
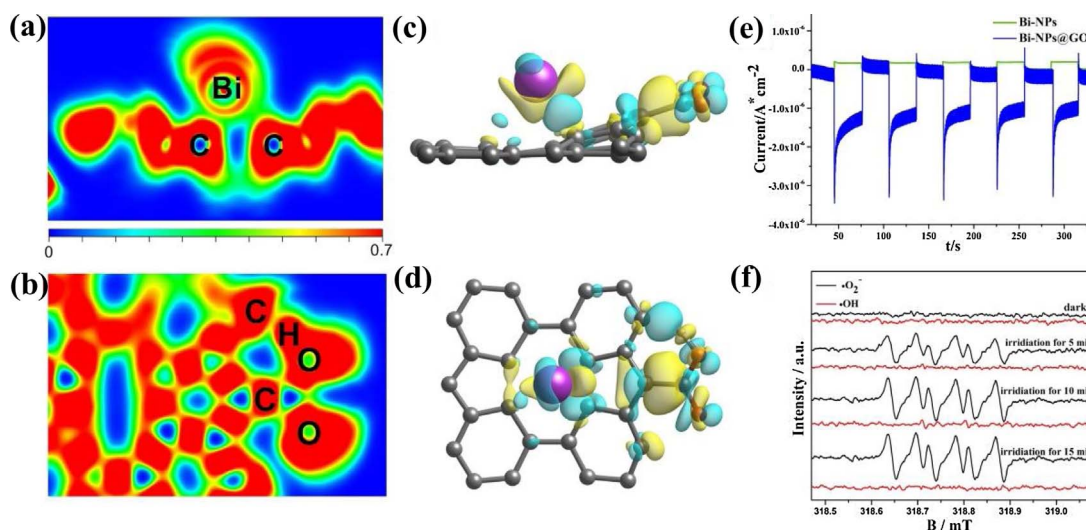
Fig. 7. The electric localization function (ELF) (a, b) and charge difference (c, d) between each atom: charge accumulation is in blue and depletion is in yellow. Red, purple and grey spheres depict O, Bi and C atoms, respectively (a and c are side view, b and d are top view).Transient photocurrent responses of Bi-NPs and Bi-NPs@GO (e), DMPO spin-trapping ESR spectra of Bi-NPs@GO in aqueous dispersion for DMPO-·OH and in methanol dispersion for DMPO-·O_2^- (f). (For interpretation of the references to colour in this figure legend, the reader is referred to the web version of this article.)

samples over that of Bi-NPs is observed, implying an enhanced transportation efficiency of photoinduced electrons after the introdcue of GO. It is believed that this enhanced transportation efficiency should be ascribed to the creation of the electron delivery channel: Bi → $C_{graphene}$ → $Atom_{COOH}$ → O_{COOH}, which drives the photo-excited electrons flowing onto the carboxy group of GO. Though there is a thin BiOx layer on the surface of Bi NPs, the photoinduced electrons could pass through the thin layer of amorphous bismuth oxide via the well-known quantum tunneling [47]. The ESR spectra of Bi-NPs@GO were carried out to identify the major active species responsible for NO removal. Under UV light irradiation, the characteristic peaks of DMPO-·O_2^- while no signal of DMPO-·OH were detedcted in Fig. 6f, indicating the main active free radical is ·O_2^-. Though the Femi level of nanostructured bismuth is −0.17eV [47], hot electrons generated with the non-radiative decay of LSPR were endowed higher reduction potential to give massive production of ·O_2^-. The leaving holes are not able to oxidize H_2O and OH^- to ·OH but directly oxdize DMPO to DMPOX, contributing to some strong extra peaks in DMPO-·O_2^- shown in Fig. 7f [48]. Also, the hot holes are active species with strong oxidizing power for photocatalytic NO oxidation via 2NO + $2h^+$ + O_2 + $4OH^-$ → $2NO_3^-$ + $2H_2O$. Thus, the photoinduced ·O_2^- and hot holes are the main reactive radicals in photocatalytic NO removal. Note that carboxyl groups are electron acceptor in Bi-NPs@GO, the ·O_2^- would be enriched on GO parts where redox reactions could be preferential to stimulate. In conclusion, GO boosts the carrier separation efficiency by attracting the photoexcited hot electrons from Bi nanospheres, and then accumulates active radicals ·O_2^- for further contaminant oxidation.

3.5. Pathway of photocatalytic NO removal

To identify the pathway of photocatalytic NO removal, the time-dependent *in situ* DRIFTS spectra of Bi-NPs and Bi-NPs@GO are collected in Fig. 8. The baseline is background value of each sample. The ad-desorption equilibrium reaches after introducing NO and O_2 in the absence of light irradiation. In adsorption period, molecule adsorbed NO_2 (1598 cm^{-1}) [49] and monodentate nitrate (1270 cm^{-1}) [50] were observed on Bi-NPs (Fig. 8a). NO_2 is obviously the product of NO oxidation by surface adsorbed oxygen. The formation of monodentate nitrates mainly due to adsorption of NO on the BiOx layer at the surface of Bi-NPs. In the case of Bi-NPs@GO, some other bands corresponding to NO^+ (2123 cm^{-1}) [51], bidentate nitrite (shoulder 1174 cm^{-1}) [52]

and bridging nitrate (1007 cm^{-1}) [53] were detected before UV irradiation (Fig. 8b). With the introduction of GO, NO molecule is prone to diffuse on carboxyl groups and adsorbed on the C=O part to form CO-(ONO), a bidentate state [54]. At the same time, the existence of carboxyl terminals could also facilitate the formation of NO^+ and bridging nitrate in adsorption period which are the key intermediate products of NO photocatalytic oxidation process.

When photocatalytic reaction begins, intensities of NO_2 (1598 cm^{-1}) and monodentate nitrate (1270 cm^{-1}) observed in adsorption time are slightly enhanced, while no other new detectable variations over Bi-NPs are observed (Fig. 8a). As the hot carrier produced via LSPR in Bi nanospheres are inherently failed in traveling over distances before losing their energy by radiative scattering and the existence of surface surfactant on Bi-NPs would also interdict remaining hot carrier transferring to some extent, no further photocatalytic reactions takes place successfully on Bi-NPs consequently. In comparison, all intensities shown in adsorption time on Bi-NPs@GO (Fig. 8b) are obviously increased as time off, except for molecular NO_2 that finally vanish in later reaction. There is a new weak negative band observed at 2012 cm^{-1} that is assigned to NO adsorbed on surface BiOx layer [52], which due to NO consumed during photocatalytic reaction gradually. As Bi-NPs@GO photoexcited by UV light, NO_2 existing in adsorption time could easily gain photogenerated hot electrons on carboxyl to create nitroso intermediates, i.e. bidentate nitrites (1528, 1411 cm^{-1}) [53] and chelated nitrites (830 cm^{-1}) [55]. According to the observation of adsorption and photocatalysis processes over Bi-NPs and Bi-NPs@GO, NO photocatalytic removal pathway can be revealed: Firstly, NO molecules are adsorbed on carboxyl groups on the edge of GO to form CO-(ONO). NO^+ and other nitroso compounds are also formed accompanying with GO in adsorption time. Then, with photocatalytic reaction begins, carboxyl groups receiving hot electrons generated along the LSPR of Bi nanospheres enrich oxygen molecules and intermediate products at the same time. As a result, all the intermediates tend to be oxidized to either monodentate (1274 cm^{-1}) or bidentate nitrate (1174 cm^{-1}) by the holes and ·O_2^- on carboxyl groups where NO photocatalytic oxidized to final products completely [56,57]. It is noteworthy that all these nitro and nitroso compounds still exist when light off, which imply that all the final products are accumulated on the surface persistently. The *in situ* DRFIT fact agrees with the extended photocatalytic activity of Bi-NPs and Bi-NPs@GO.

According to the charge density difference (Fig. 7c,d), the existence of GO could promote the carrier separation efficiency by dragging the
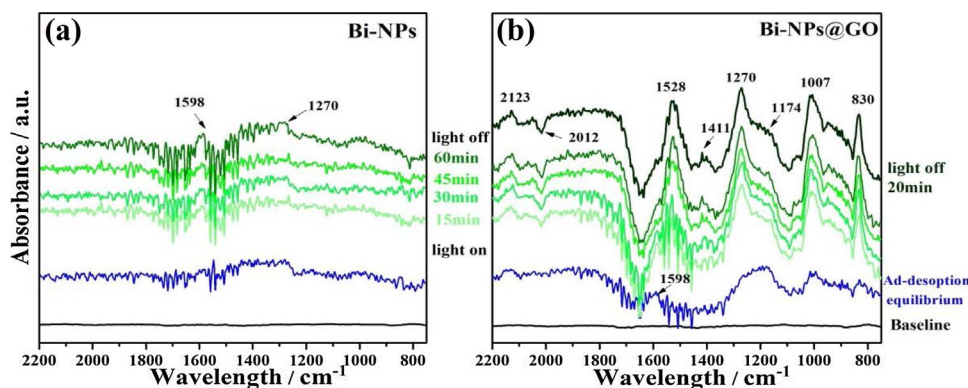
Fig. 8. *In situ* DRIFTS spectra of photocatalytic reaction of NO on Bi-NPs (a) and Bi-NPs@GO (b) under UV light irradiation.

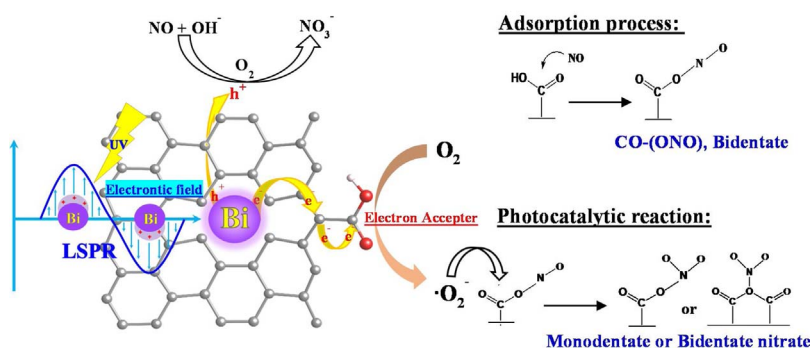Pathway of photocatalytic NO oxidation on Bi-NPs@GO

Fig. 9. Schematic diagram of the directed carrier transfer channel and NO removal pathway on carboxyl of Bi-NPs@GO.

photoexcited SPR hot electrons from Bi nanospheres to carboxyl groups, thus massive $\cdot O_2^-$ as the active species are accumulated on carboxyl groups. Besides, NO molecules are adsorbed on carboxyl groups on the edge of GO to form CO-(ONO) which is an important intermediate via *in situ* DRFIT monitor (Fig. 8a,b). Thus, carboxyl groups in GO actually function as both adsorption and reaction centers in photocatalytic NO oxidation.

Schematic diagram of the carrier transfer channel and NO removal pathway on carboxyl of Bi-NPs@GO are shown in Fig. 9. The nitric oxides compounds are much more populated on carbon surface in the reacting stream. Carboxyl groups on GO undoubtedly play as adsorption and reaction centers in photocatalytic NO removal.

4. Conclusion

In summary, Bi nanospheres (Bi-NPs) with uniform size and morphology were successfully fabricated. The as prepared Bi-NPs were then assembled onto GO sheets to get the resultant Bi-NPs@GO which exhibits excellent photocatalytic activity and stability for ppb-level NO removal. Energetic hot electrons produced via LSPR effect of Bi nanospheres provide unique reaction pathways for NO oxidation. The existence of GO could advance the carrier separation efficiency by dragging the photoexcited hot electrons from Bi nanospheres to carboxyl groups where active radicals $\cdot O_2^-$ are accumulated. Carboxyl groups in GO work as both adsorption and reaction centers in photocatalytic NO oxidation via *in situ* DRFIT monitored. This present work could not only provide an available thought of direct plasmonic photocatalysis but open an available way for enhancement of electronic separation efficiency.

Acknowledgements

Appendix A. Supplementary data

Supplementary data associated with this article can be found, in the online version, at http://dx.doi.org/10.1016/j.apcatb.2017.09.046.

References

[1] M.J. Kale, T. Avanesian, P. Christopher, Direct photocatalysis by plasmonic nanostructures, ACS Catal. 4 (2013) 116–128.
[2] F. Dong, T. Xiong, Y. Sun, L. Lu, Y. Zhang, H. Zhang, H. Huang, Y. Zhou, Z. Wu, Exploring the photocatalysis mechanism on insulators, Appl. Catal. B: Environ. 219 (2017) 450–458.
[3] G. Jiang, X. Li, M. Lan, T. Shen, X. Lv, F. Dong, S. Zhang, Monodisperse bismuth nanoparticles decorated graphitic carbon nitride: enhanced visible-light-response photocatalytic NO removal and reaction pathway, Appl. Catal. B: Environ. 205 (2017) 532–540.
[4] R. Sundararaman, P. Narang, A.S. Jermyn, W.A. Goddard III, H.A. Atwater, Theoretical predictions for hot-carrier generation from surface plasmon decay, Nat. Commun. 5 (2014) 5788.
[5] J. Ma, Z. Wang, L.-W. Wang, Interplay between plasmon and single-particle excitations in a metal nanocluster, Nat. Commun. 6 (2015) 10107.
[6] V. Giannini, A.I. Fernández-Domínguez, S.C. Heck, S.A. Maier, Plasmonic nanoantennas: fundamentals and their use in controlling the radiative properties of nanoemitters, Chem. Rev. 111 (2011) 3888–3912.
[7] E. Cortés, W. Xie, J. Cambiasso, A.S. Jermyn, R. Sundararaman, P. Narang, S. Schlücker, S.A. Maier, Plasmonic hot electron transport drives nano-localized chemistry, Nat. Commun. 8 (2017) 14880.
[8] M.L. Brongersma, N.J. Halas, P. Nordlander, Plasmon-induced hot carrier science and technology, Nat. Nanotechnol. 10 (2015) 25–34.
[9] J.B. Khurgin, How to deal with the loss in plasmonics and metamaterials, Nat. Nanotechnol. 10 (2015) 2–6.

[10] S.C. Warren, E. Thimsen, Plasmonic solar water splitting, Energy Environ. Sci. 5 (2012) 5133–5146.

[11] P.V. Kamat, Photophysical, photochemical and photocatalytic aspects of metal nanoparticles, ChemInform (2002) 7729–7744.

[12] P. Christopher, H. Xin, A. Marimuthu, S. Linic, Singular characteristics and unique chemical bond activation mechanisms of photocatalytic reactions on plasmonic nanostructures, Nat. Mater. 11 (2012) 1044–1050.

[13] Z. Ni, W. Zhang, G. Jiang, X. Wang, Z. Lu, Y. Sun, X. Li, Y. Zhang, F. Dong, Enhanced plasmonic photocatalysis of SiO_2@Bi microspheres with hot electrons transportation channel via Bi-O-Si linkage, Chin. J. Catal. 38 (2017) 1174–1183.

[14] F. Dong, T. Xiong, Y. Sun, Z. Zhao, Y. Zhou, X. Feng, Z. Wu, A semimetal bismuth element as a direct plasmonic photocatalyst, Chem. Commun. 50 (2014) 10386–10389.

[15] C. Clavero, Plasmon-induced hot-electron generation at nanoparticle/metal-oxide interfaces for photovoltaic and photocatalytic devices, Nat. Photonics 8 (2014) 95–103.

[16] J. Toudert, R. Serna, M. Jimenez de Castro, Exploring the optical potential of nano-bismuth: tunable surface plasmon resonances in the near ultraviolet-to-near in-frared range, J. Phys. Chem. C 116 (2012) 20530–20539.

[17] E. Rokhsat, O. Akhavan, Improving the photocatalytic activity of graphene oxide/ZnO nanorod films by UV irradiation, Appl. Surf. Sci. 371 (2016) 590–595.

[18] N. Haghighi, R. Hallaj, A. Salimi, Immobilization of glucose oxidase onto a novel platform based on modified TiO_2 and graphene oxide direct electrochemistry, cat-alytic and photocatalytic activity, Mater. Sci. Eng.: C 73 (2016) 417–424.

[19] N. Wang, Y. Zhou, C. Chen, L. Cheng, H. Ding, A g-C_3N_4 supported graphene oxide/Ag_3PO_4 composite with remarkably enhanced photocatalytic activity under visible light, Catal. Commun. 73 (2016) 74–79.

[20] W. Wan, S. Yu, F. Dong, Q. Zhang, Y. Zhou, Efficient C_3N_4/graphene oxide mac-roscopic aerogel visible-light photocatalyst, J. Mater. Chem. A 4 (2016) 7823–7829.

[21] Q. Su, S. Pang, V. Alijani, C. Li, X. Feng, K. Müllen, Composites of graphene with large aromatic molecules, Adv. Mater. 21 (2009) 3191–3195.

[22] G. Zhang, B. Kirk, L.A. Jauregui, H. Yang, X. Xu, Y.P. Chen, Y. Wu, Rational synthesis of ultrathin n-type Bi_2Te_3 nanowires with enhanced thermoelectric properties, Nano Lett. 12 (2011) 56–60.

[23] S. Grimme, Semiempirical GGA-type density functional constructed with a long-range dispersion correction, J. Comput. Chem. 27 (2006) 1787–1799.

[24] G. Kresse, J. Furthmüller, Efficient iterative schemes for ab initio total-energy cal-culations using a plane-wave basis set, Phys. Rev. B 54 (1996) 11169.

[25] G. Kresse, J. Furthmüller, Efficiency of ab-initio total energy calculations for metals and semiconductors using a plane-wave basis set, Comput. Mater. Sci. 6 (1996) 15–50.

[26] J.P. Perdew, K. Burke, M. Ernzerhof, Generalized gradient approximation made simple, Phys. Rev. Lett. 77 (1996) 3865.

[27] P.E. Blöchl, Projector augmented-wave method, Phys. Rev. B 50 (1994) 17953.

[28] G. Kresse, D. Joubert, From ultrasoft pseudopotentials to the projector augmented-wave method, Phys. Rev. B 59 (1999) 1758.

[29] S.K. Bhatia, A.L. Myers, Optimum conditions for adsorptive storage, Langmuir 22 (2006) 1688–1700.

[30] R.C. Lochan, M. Head-Gordon, Computational studies of molecular hydrogen binding affinities: the role of dispersion forces, electrostatics, and orbital interac-tions, Phys. Chem. Chem. Phys. 8 (2006) 1357–1370.

[31] T.J. Bruno, P.D. Svoronos, CRC Handbook of Basic Tables for Chemical Analysis, CRC press, 2003.

[32] R.A. Patil, M.-K. Wei, P.-H. Yeh, J.-B. Liang, W.-T. Gao, J.-H. Lin, Y. Liou, Y.-R. Ma, Size-controllable synthesis of Bi/Bi_2O_3 heterojunction nanoparticles using pulsed Nd: YAG laser deposition and metal–semiconductor-heterojunction-assisted photo-luminescence, Nanoscale 8 (2016) 3565–3571.

[33] M. Halik, H. Klauk, U. Zschieschang, G. Schmid, S. Ponomarenko, S. Kirchmeyer, W. Weber, Relationship between molecular structure and electrical performance of oligothiophene organic thin film transistors, Adv. Mater. 15 (2003) 917–922.

[34] T. Jung, A. Dodabalapur, R. Wenz, S. Mohapatra, Moisture induced surface polar-ization in a poly (4-vinyl phenol) dielectric in an organic thin-film transistor, Appl. Phys. Lett. 87 (2005) 182109.

[35] E. Díaz, R.B. Valenciano, I.A. Katime, Study of complexes of poly (vinyl pyrrolidone) with copper and cobalt on solid state, J. Appl. Polym. Sci. 93 (2004) 1512–1518.

[36] N.-F. Chiu, S.-Y. Fan, C.-D. Yang, T.-Y. Huang, Carboxyl-functionalized graphene oxide composites as SPR biosensors with enhanced sensitivity for immunoaffinity detection, Biosens. Bioelectron. 89 (2017) 370–376.

[37] M. Acik, G. Lee, C. Mattevi, A. Pirkle, R.M. Wallace, M. Chhowalla, K. Cho, Y. Chabal, The role of oxygen during thermal reduction of graphene oxide studied by infrared absorption spectroscopy, J. Phys. Chem. C 115 (2011) 19761–19781.

[38] G. Bugnon, G. Parascandolo, T. Söderström, P. Cuony, M. Despeisse, S. Hänni, J. Holovský, F. Meillaud, C. Ballif, A new view of microcrystalline silicon: the role of plasma processing in achieving a dense and stable absorber material for photo-voltaic applications, Adv. Funct. Mater. 22 (2012) 3665–3671.

[39] M. Li, S.K. Cushing, X. Zhou, S. Guo, N. Wu, Fingerprinting photoluminescence of functional groups in graphene oxide, J. Mater. Chem. 22 (2012) 23374–23379.

[40] X. Li, H. Wang, J.T. Robinson, H. Sanchez, G. Diankov, H. Dai, Simultaneous ni-trogen doping and reduction of graphene oxide, J. Am. Chem. Soc. 131 (2009) 15939–15944.

[41] W.Z. Wang, B. Poudel, Y. Ma, Z. Ren, Shape control of single crystalline bismuth nanostructures, J. Phys. Chem. B 110 (2006) 25702–25706.

[42] G. Jiang, Z. Lin, C. Chen, L. Zhu, Q. Chang, N. Wang, W. Wei, H. Tang, TiO_2 na-noparticles assembled on graphene oxide nanosheets with high photocatalytic ac-tivity for removal of pollutants, Carbon 49 (2011) 2693–2701.

[43] K. Singh, A. Ohlan, V.H. Pham, R. Balasubramaniyan, S. Varshney, J. Jang, S.H. Hur, W.M. Choi, M. Kumar, S. Dhawan, Nanostructured graphene/Fe_3O_4 in-corporated polyaniline as a high performance shield against electromagnetic pol-lution, Nanoscale 5 (2013) 2411–2420.

[44] D. Cai, M. Song, Preparation of fully exfoliated graphite oxide nanoplatelets in organic solvents, J. Mater. Chem. 17 (2007) 3678–3680.

[45] J. Huo, H. Song, X. Chen, B. Cheng, From carbon-encapsulated iron nanorods to carbon nanotubes, J. Phys. Chem. C 112 (2008) 5835–5839.

[46] Z. Wei, L. Rosa, K. Wang, M. Endo, S. Juodkazis, B. Ohtani, E. Kowalska, Size-controlled gold nanoparticles on octahedral anatase particles as efficient plasmonic photocatalyst, Appl. Catal. B: Environ. 206 (2017) 393–405.

[47] F. Dong, Z. Zhao, Y. Sun, Y. Zhang, S. Yan, Z. Wu, An advanced semimetal–organic Bi Spheres–g-C_3N_4 nanohybrid with SPR-enhanced visible-light photocatalytic performance for NO purification, Environ. Sci. Technol. 49 (2015) 12432–12440.

[48] R.A. Floyd, L.M. Soong, Spin trapping in biological systems. Oxidation of the spin trap 5, 5-dimethyl-1-pyrroline-1-oxide by a hydroperoxide-hematin system, Biochem. Biophys. Res. Commun. 74 (1977) 79–84.

[49] L. Sivachandiran, F. Thevenet, A. Rousseau, D. Bianchi, NO_2 adsorption mechanism on TiO_2: An in-situ transmission infrared spectroscopy study, Appl. Catal. B: Environ. 198 (2016) 411–419.

[50] D. Pozdnyakov, V. Filimonov, Infrared spectroscopic study of the chemisorption of nitric oxide and nitrogen dioxide on metal oxides, Kinet. Katal 14 (1973) 760–766.

[51] K. Hadjiivanov, J. Saussey, J. Freysz, J. Lavalley, FT-IR study of NO + O_2 co-ad-sorption on H-ZSM-5: re-assignment of the 2133 cm^{-1} band to NO^+ species, Catal. Lett. 52 (1998) 103–108.

[52] J.C. Wu, Y.-T. Cheng, In situ FTIR study of photocatalytic NO reaction on photo-catalysts under UV irradiation, J. Catal. 237 (2006) 393–404.

[53] K. Hadjiivanov, V. Bushev, M. Kantcheva, D. Klissurski, Infrared spectroscopy study of the species arising during nitrogen dioxide adsorption on titania (anatase), Langmuir 10 (1994) 464–471.

[54] H. Teng, Y.T. Tu, Y.C. Lai, C.C. Lin, Reduction of NO with NH_3 over carbon cata-lysts: the effects of treating carbon with H_2SO_4 and HNO_3, Carbon 39 (2001) 575–582.

[55] B. Klingenberg, M. Vannice, NO adsorption and decomposition on La_2O_3 studied by DRIFTS, Appl. Catal. B: Environ. 21 (1999) 19–33.

[56] Z. Wang, S. Yan, Y. Sun, T. Xiong, F. Dong, W. Zhang, Bi metal sphere/graphene oxide nanohybrids with enhanced direct plasmonic photocatalysis, Appl. Catal. B: Environ. 214 (2017) 148–157.

[57] X. Li, Y. Sun, T. Xiong, G. Jiang, Y. Zhang, Z. Wu, F. Dong, Activation of amorphous bismuth oxide via plasmonic Bi metal for efficient visible-light photocatalysis, J. Catal. 352 (2017) 102–112.